Monthly Notices
of the
ROYAL ASTRONOMICAL SOCIETY

MNRAS **447,** 2821–2835 (2015) doi:10.1093/mnras/stu2628

General relativistic neutron stars with twisted magnetosphere

A. G. Pili,[1,2,3]★ N. Bucciantini[2,3] and L. Del Zanna[1,2,3]

[1]*Dipartimento di Fisica e Astronomia, Università degli Studi di Firenze, Via G. Sansone 1, I-50019 Sesto F. no (Firenze), Italy*
[2]*INAF, Osservatorio Astrofisico di Arcetri, Largo E. Fermi 5, I-50125 Firenze, Italy*
[3]*INFN, Sezione di Firenze, Via G. Sansone 1, I-50019 Sesto F. no (Firenze), Italy*

Accepted 2014 December 10. Received 2014 December 9; in original form 2014 June 30

ABSTRACT

Soft gamma-ray repeaters and anomalous X-ray pulsars are extreme manifestations of the most magnetized neutron stars: magnetars. The phenomenology of their emission and spectral properties strongly support the idea that the magnetospheres of these astrophysical objects are tightly twisted in the vicinity of the star. Previous studies on equilibrium configurations have so far focused on either the internal or the external magnetic field configuration, without considering a real coupling between the two fields. Here, we investigate numerical equilibrium models of magnetized neutron stars endowed with a confined twisted magnetosphere, solving the general relativistic Grad–Shafranov equation both in the interior and in the exterior of the compact object. A comprehensive study of the parameters space is provided, to investigate the effects of different current distributions on the overall magnetic field structure.

Key words: gravitation – MHD – stars: magnetars – stars: magnetic field – stars: neutron.

1 INTRODUCTION

Neutron stars (NSs) can manifest themselves as different classes of astrophysical sources, each one of them characterized by a peculiar phenomenology. Among these classes, anomalous X-ray pulsars (AXPs) and soft gamma-ray repeaters (SGRs) are particularly remarkable because of their extraordinary energetic properties. Both exhibit a persistent X-ray emission with luminosities $L_X \sim 10^{33}$–10^{36} ergs^{-1}. They are characterized by flaring activity with X-ray bursts whose duration is ∼0.1–1 s and with peak luminosities ∼10^{40}–10^{41}ergs^{-1} which are, in some cases, associated also with a pulsed radio transient emission. SGRs are sources of violent events, known as giant flares, during which an amount of energy ∼10^{44}–10^{46} erg is released (for recent reviews, see Mereghetti 2008; Rea & Esposito 2011; Turolla & Esposito 2013).

There is a general consensus that SGRs and AXPs, on the ground of their observational properties, are part of a same class of NSs called *magnetars* (Duncan & Thompson 1992; Thompson & Duncan 1993). These are young (with a typical age of 10^4 yr), isolated NSs with rotational period in the range ∼2–12 s, and with a typical dipole magnetic field, inferred from spin-down, in the range 10^{14}–10^{15} G (Kouveliotou et al. 1999). Since they are slow rotators, spin-down energy losses cannot power their emission, which is instead believed to originate in the magnetic energy stored in the interior. The observed phenomenology would be thus sustained by the rearrangement and dissipation of their huge magnetic fields.

The simultaneous presence of high density, strong gravity, and strong magnetic fields makes magnetars a unique environment. Unfortunately, it is not yet known how such a strong magnetic field can form, and even less known are the requirements for its stability. During the collapse of the progenitor star and the formation of the compact proto-NS, any fossil field, inherited by the progenitor, can be either enhanced by the compression of the core (Spruit 2009) or/and by its differential rotation. It is not clear, however, if this is enough to achieve the typical magnetar field strengths, or if some form of dynamo is necessary (Thompson & Duncan 1993; Bonanno, Rezzolla & Urpin 2003; Rheinhardt & Geppert 2005; Burrows et al. 2007). In this case, protomagnetars should be born as millisecond rotators, with important consequences for the supernova explosion itself (Bucciantini et al. 2009; Metzger et al. 2011; Bucciantini et al. 2012).

In any case, there is no reason to expect that the magnetic field, at the very beginning, is already in a stable configuration, while it is more likely expected that it will rapidly evolve into a stable one. This is because the Alfvénic crossing time is much smaller than the typical Kelvin–Helmholtz time-scale (Pons et al. 1999). After ∼100 s since the formation of the proto-NS, the neutrino-driven wind ceases. This is the typical time when an approximatively force-free magnetosphere can be established outside the star. It is also the time when a crust begins to form, eventually freezing the magnetic field on the NS surface. From now on, the magnetic fields evolve on the much longer diffusive time-scale (Braithwaite & Spruit 2006; Gourgouliatos et al. 2013; Viganò et al. 2013).

The study of the properties of magnetic configurations inside NSs is thus an important step towards a complete understanding of magnetars and their properties. It is well known that either purely poloidal or purely toroidal magnetic configurations are highly unstable (Prendergast 1956; Lander & Jones 2011a,b; Ciolfi & Rezzolla 2012). However, given their simplicity, such kind of configurations

★ E-mail: pili@arcetri.astro.it

have been extensively investigated in the context of equilibrium models of magnetized NSs either in the Newtonian regime, from the earlier studies of Chandrasekhar & Fermi (1953) to the more recent Yoshida, Yoshida & Eriguchi (2006), or in full General Relativity (GR) by Bocquet et al. (1995), Kiuchi & Yoshida (2008), Frieben & Rezzolla (2012) and Pili, Bucciantini & Del Zanna (2014, hereafter PBD14).

Stability was investigated by Braithwaite & Nordlund (2006) and Braithwaite (2009) by means of numerical simulations in the Newtonian magnetohydrodynamic (MHD) regime. The general outcome of the relaxation of the initial magnetic field is a dynamically stable *Twisted Torus* (TT) configuration, where the poloidal field is roughly axisymmetrically twined with a toroidal field, of comparable strength, into a ring-like region located just underneath the surface of the star. The exterior field they find is mainly a dipole with only smaller contributions from higher order multipoles (note however that they impose a potential field outside the NS surface, confining any current to the interior).

Given that TT configurations seem in principle to be stable, particular efforts have been recently aimed at their investigation. Models have been worked out in the Newtonian regime (Lander & Jones 2009; Fujisawa, Yoshida & Eriguchi 2012; Glampedakis, Andersson & Lander 2012), in GR with a perturbative approach (Ciolfi et al. 2009; Ciolfi, Ferrari & Gualtieri 2010; Ciolfi & Rezzolla 2013) and more recently also in the fully non-linear GR regime in PBD14.

The analysis of equilibrium configurations has mainly focused on understanding the effects of the magnetic field on the structure of the star. Strong magnetic fields, indeed, could deform the star, and such deformations, in conjunction with fast rotation, could lead to emission of gravitational waves (GW) which, in principle, would be observed by the next generation of ground-based detectors (Mastrano et al. 2011; Lasky & Melatos 2013). This makes strongly magnetized NS prime candidates for GW detection. Moreover, there are some recent claims of a free precession in 4U 0142+61 suggesting a prolate deformation of the NS, possibly caused by a toroidal magnetic field of the order of 10^{16} G (Makishima et al. 2014).

Until now, NS equilibrium models have been developed assuming that the star is surrounded by a 'vacuum'. However, since the seminal work of Goldreich & Julian (1969), it is clear that rotating NSs are actually surrounded by a magnetosphere filled by a charge-separated, low-pressure plasma. Since the plasma pressure and its mass density are negligible with respect to the electromagnetic energy density, the magnetosphere can be described in the force-free approximation (Contopoulos, Kazanas & Fendt 1999; Spitkovsky 2006; Kalapotharakos & Contopoulos 2009; Contopoulos, Kalapotharakos & Kazanas 2014; Philippov, Tchekhovskoy & Li 2014).

In the case of magnetars, we expect that their magnetosphere is endowed with a high twisted magnetic field. This is strongly suggested by the features of their persistent X-ray spectra, which are well fitted by a blackbody-like component at $kT \sim 0.5$ keV, joined with a power-law tail that becomes dominant above 10 keV (Kuiper et al. 2006). The latter can be explained in terms of resonant cyclotron scattering of the thermal photons by magnetospheric particles as proposed in Thompson, Lyutikov & Kulkarni (2002) and Beloborodov & Thompson (2007). These authors pointed out that the dissipation of magnetic energy inside the star could induce a twist of the emergent magnetic field into a non-potential state which is sustained by electric currents that, threading the magnetosphere, might interact with the thermal photons emitted by the surface of the NSs.

The twisted magnetosphere scenario has been successfully validated by calculation of synthetic spectra (Lyutikov & Gavriil 2006; Fernández & Thompson 2007; Nobili, Turolla & Zane 2008; Taverna et al. 2014). These works show that the morphology of the external magnetic field, and the related charge distributions, highly affect the spectral shape and the pulse profile of the emitted radiation. This indicates the importance of a correct modelling and understanding of global magnetic configurations. Typically, the standard reference model is the one discussed in Thompson et al. (2002), where extending previous works on the solar corona (Low & Lou 1990; Wolfson 1995) to NSs, the magnetosphere is described in terms of a self-similar, globally twisted, dipolar magnetic field. This model has been refined to account for higher order multipoles by Pavan et al. (2009), in response to observational indications of a local, rather than global, twist in the magnetosphere (Woods et al. 2007; Perna & Gotthelf 2008). Recently, this scenario has been strengthened also by the detection of a proton cyclotron feature in the X-ray spectrum of the 'low-field' magnetar SGR 0418+5729 which is compatible with a strong, but localized, toroidal field of the order of 10^{15} G (Tiengo et al. 2013). More general equilibrium models have been obtained by Viganò, Pons & Miralles (2011) using a magnetofrictional method, also first developed in the context of the solar corona studies (Yang, Sturrock & Antiochos 1986; Roumeliotis, Sturrock & Antiochos 1994), or by Parfrey, Beloborodov & Hui (2013) who, with time-dependent numerical simulations, investigated the response of the magnetosphere to different shearing profiles of the magnetic footpoints.

Given the complexity of the problem, until very recently studies have focused either on the internal field structure (assuming a prescription for the magnetosphere) or on the external magnetosphere (assuming an internal current distribution). It is obvious that the two cannot be worked out independently, and global models are the necessary step forward. A first attempt in this direction has been recently made in Glampedakis, Lander & Andersson (2014). Considering non-rotating stars in Newtonian regime, they show that a 'Grad–Shafranov (GS) approach' to the problem can be used to obtain global equilibrium configurations, with twists and currents extending from the interior to the magnetosphere. A different approach was used in Ruiz, Paschalidis & Shapiro (2014), where for the first time, detailed GR models of pulsar magnetosphere were developed. In particular, they search for steady state configurations by evolving in time the NS and by matching the interior field, treated with ideal MHD equation, to the exterior force-free solution.

In this work we extend previous results, and present for the first time GR models of NSs endowed with a twisted magnetic field, threading both the interior and the outer magnetosphere. Models are derived from the solution of the general relativistic GS equation, both in the interior and in the exterior of the star. Our results are a generalization of the TT models presented in PBD14, that allow electric currents to flow outside the star. We have investigated several models, varying either the strength of the currents producing the twist in the magnetosphere, or the extent of the magnetosphere itself. Extending the work of Glampedakis et al. (2014), where a couple of typical configurations were presented, we develop a detailed study of the parameter space. We investigate how currents are distributed and how they affect the topology of the resulting magnetic field. We show the modifications expected on the shape of the field at the surface, the magnetic dipole moment, and the energy stored in the toroidal component of the magnetic field.

The paper is organized as follows. In Section 2, we present the mathematical framework adopted, and our choice for the currents defining the magnetosphere. In Section 3, we describe the numerical

setup. In Section 4, we present and discuss our models, and finally we conclude in Section5. In the following, we assume a signature $(-,+,+,+)$ for the space–time metric, employing Latin letters $i, j, k, \ldots$ (running from 1 to 3) for 3D spatial tensor components. We set $c = G = 1$ and all $\sqrt{4\pi}$ factors are absorbed in the definition of the electromagnetic fields.

2 FORMALISM

All our magnetized NS models will be assumed here as non-rotating (as previously discussed, magnetars have a long rotation period) and axisymmetric. Ideal, General Relativistic Magnetohydrodynamics (GRMHD) is supposed to hold in the interior of the star, and it is also assumed to hold in the external magnetosphere, where plasma inertia is certainly negligible (this actually corresponds to the so-called force-free regime). Our formalism follows the notation used in PBD14, to which the reader is referred for a more complete discussion.

2.1 The GRMHD Grad–Shafranov equation

When the stress-energy tensor describing the matter distribution and the magnetic field of a NS is axisymmetric, then the space–time itself must retain the same symmetry (Carter 1970, 1973). As we showed in PBD14, NS models in full GR can be conveniently computed, preserving a high accuracy, in the so-called *conformally flat approximation* for the space–time metric (Wilson, Mathews & Marronetti 1996; Wilson & Mathews 2003). This allows one to notably simplify Einstein equations recasting them in a numerical stable form, and yet to derive results that are fully consistent (with typical relative errors $\sim 10^{-4}$) with more sophisticated approaches to GR (Cordero-Carrión et al. 2009; Bucciantini & Del Zanna 2011). In the case of a static non-rotating star the line element of a conformally flat space–time is written, using spherical like coordinates (t, r, θ, ϕ), as

$$\mathrm{d}s^2 = -\alpha^2 \mathrm{d}t^2 + \psi^4(\mathrm{d}r^2 + r^2\mathrm{d}\theta^2 + r^2\sin^2\theta\,\mathrm{d}\phi^2), \tag{1}$$

where α is the *lapse function* and ψ is the *conformal factor*, dependent on the position. We note that, since we consider a non-rotating star, the line element does not contain any mixed term $\mathrm{d}x^i\mathrm{d}t$, corresponding to a vanishing *shift vector* $\beta^i = 0$ in the $3+1$ formalism. Both the metric functions α and ψ are obtained solving Einstein equations that, in the specific case of conformal flatness and a static NS, reduce to a set of two non-linear elliptic partial differential equations (PDEs; see PBD14 or Bucciantini & Del Zanna 2011).

In an axisymmetric and static space–time the electromagnetic field can be described uniquely in terms of a magnetic potential, which coincides with the covariant ϕ component of the vector potential A_ϕ, and it is usually referred to as the *magnetic flux function*. In particular, the solenoidality condition, together with axisymmetry, allows one to express the poloidal component of the magnetic field as a gradient of the magnetic flux function, whereas the toroidal counterpart is related to A_ϕ by means of a free scalar *current function* $\mathcal{I}$ that depends on A_ϕ alone. Thus, under the assumption of a conformally flat metric, the components of the magnetic field are given by

$$B^r = \frac{\partial_\theta A_\phi}{\psi^6 r^2 \sin\theta}, \quad B^\theta = -\frac{\partial_r A_\phi}{\psi^6 r^2 \sin\theta}, \quad B^\phi = \frac{\mathcal{I}(A_\phi)}{\alpha\psi^4 r^2 \sin^2\theta}. \tag{2}$$

From the static GRMHD system, in the presence of an external magnetic field and assuming a barotropic equation of state (EoS) for the fluid, the Euler equation can be written as

$$\partial_i \ln h + \partial_i \ln\alpha = \frac{\mathrm{d}\mathcal{M}}{\mathrm{d}A_\phi}\partial_i A_\phi, \tag{3}$$

where ρ is the rest mass density, $h := (e+p)/\rho$ is the specific enthalpy, e and p are the energy density and the thermal pressure, respectively. Here, we have already related the Lorentz force component L_i to the gradient of the *magnetization function* $\mathcal{M}(A_\phi)$ through

$$\rho h \partial_i \mathcal{M} = L_i = \epsilon_{ijk} J^j B^k, \tag{4}$$

in which $J^i = \alpha^{-1}\epsilon^{ijk}\partial_j(\alpha B_k)$ are the conduction currents that can be expressed, in terms of $\mathcal{I}$ and $\mathcal{M}$, with

$$J^r = \alpha^{-1}B^r\frac{\mathrm{d}\mathcal{I}}{\mathrm{d}A_\phi}, \quad J^\theta = \alpha^{-1}B^\theta\frac{\mathrm{d}\mathcal{I}}{\mathrm{d}A_\phi},$$
$$J^\phi = \rho h\frac{\mathrm{d}\mathcal{M}}{\mathrm{d}A_\phi} + \frac{\mathcal{I}}{\varpi^2}\frac{\mathrm{d}\mathcal{I}}{\mathrm{d}A_\phi}, \tag{5}$$

where we have defined $\varpi := \alpha\psi^2 r\sin\theta$.

Integrating equation (3) one obtains the *Bernoulli integral*

$$\ln\left(\frac{h}{h_c}\right) + \ln\left(\frac{\alpha}{\alpha_c}\right) - \mathcal{M} = 0, \tag{6}$$

which, once the functional form of $\mathcal{M}$ has been chosen and both α and A_ϕ are available, relates the enthalpy at each point to the conditions set at the centre of the star (labelled c), where we assume $\mathcal{M}_c = 0$. Finally, the magnetic flux function A_ϕ is related to the metric terms and the hydrodynamical quantities through the GRMHD GS equation

$$\tilde{\Delta}_3\tilde{A}_\phi + \frac{\partial A_\phi \partial\ln(\alpha\psi^{-2})}{r\sin\theta} + \psi^8 r\sin\theta\left(\rho h\frac{\mathrm{d}\mathcal{M}}{\mathrm{d}A_\phi} + \frac{\mathcal{I}}{\varpi^2}\frac{\mathrm{d}\mathcal{I}}{\mathrm{d}A_\phi}\right) = 0. \tag{7}$$

This is obtained by working out the derivatives of the magnetic field in equation (4) introducing, for convenience, the new variable $\tilde{A}_\phi = A_\phi/(r\sin\theta)$ and the following differential operators

$$\tilde{\Delta}_3 := \Delta - \frac{1}{r^2\sin^2\theta} = \partial_r^2 + \frac{2}{r}\partial_r + \frac{1}{r^2}\partial_\theta^2 + \frac{1}{r^2\tan\theta}\partial_\theta - \frac{1}{r^2\sin^2\theta}, \tag{8}$$

$$\partial f\partial g := \partial_r f\partial_r g + \frac{1}{r^2}\partial_\theta f\partial_\theta g. \tag{9}$$

The GS equation, which governs the GRMHD equilibrium inside the star, can be extended also outside if we describe the external magnetosphere as a low-density plasma where the force-free regime is valid. Indeed, in the non-rotating case, the force-free condition reduces to the vanishing of the Lorentz force $L_i = 0$, and one can again obtain a GS equation that corresponds to equation (7) in the $\rho \to 0$ limit. We notice that taking the non-relativistic limit of equation (7) with $\rho \to 0$ leads to the non-rotating limit of the so-called pulsar equation (Glampedakis et al. 2014).

Finally, we recall that our choice of expressing all the electromagnetic quantities as functions of A_ϕ is not appropriate in the case of a purely toroidal magnetic field, which instead requires a different description, see PBD14 or Gourgoulhon et al. (2011) for details.

2.2 Choice of the free functions

The current and magnetization free functions entering the GS equation can be easily modified, with respect to the choice made in PBD14, in order to allow the currents to flow also outside the star. We can actually retain the same form for the magnetization function $\mathcal{M}$

$$\mathcal{M}(A_\phi) = k_{\rm pol} A_\phi, \tag{10}$$

where $k_{\rm pol}$ is the *poloidal magnetization constant*, while we adopt here a different functional form for $\mathcal{I}$, namely

$$\mathcal{I}(A_\phi) = \frac{a}{\zeta+1}\Theta\left[A_\phi - A_\phi^{\rm ext}\right]\frac{\left(A_\phi - A_\phi^{\rm ext}\right)^{\zeta+1}}{\left(A_\phi^{\rm max}\right)^{\zeta+1/2}}, \tag{11}$$

where $\Theta[.]$ is the Heaviside function, $A_\phi^{\rm max}$ is the maximum value that the ϕ component of the vector potential reaches over the entire domain, while $A_\phi^{\rm ext}$ is the maximum value it reaches at a distance $r = \lambda r_{\rm e}$ from the star (being $r_{\rm e}$ the equatorial radius). We further define a as the *toroidal magnetization constant*, whereas ζ is the *toroidal magnetization index*. Note that these choices are analogous to the ones made in Glampedakis et al. (2014). The new parameter λ, that enters in the definition of $A_\phi^{\rm ext}$, allows us to control the size of the twisted magnetosphere outside the star. The results of PBD14 are recovered assuming $\lambda = 1$. On the other hand, for $\lambda > 1$ the toroidal magnetic field is not confined within the star but extends smoothly outside the stellar surface, just like the poloidal component.

From the relations (5), given our choice for the free functions $\mathcal{M}$ and $\mathcal{I}$, the components of the conduction currents become

$$J^r = \alpha^{-1} B^r\, a\Theta\left[A_\phi - A_\phi^{\rm ext}\right]\frac{\left(A_\phi - A_\phi^{\rm ext}\right)^{\zeta}}{\left(A_\phi^{\rm max}\right)^{\zeta+1/2}}, \tag{12}$$

$$J^\theta = \alpha^{-1} B^\theta\, a\Theta\left[A_\phi - A_\phi^{\rm max}\right]\frac{\left(A_\phi - A_\phi^{\rm ext}\right)^{\zeta}}{\left(A_\phi^{\rm max}\right)^{\zeta+1/2}}, \tag{13}$$

$$J^\phi = \rho h\, k_{\rm pol} + \frac{a^2}{(\zeta+1)\varpi^2}\Theta\left[A_\phi - A_\phi^{\rm ext}\right]\frac{\left(A_\phi - A_\phi^{\rm ext}\right)^{2\zeta+1}}{\left(A_\phi^{\rm max}\right)^{2\zeta+1}}. \tag{14}$$

Note that, thanks to the renormalization by $A_\phi^{\rm max}$, the ϕ component of the conduction current is independent from the absolute value of the magnetic flux function (it does not depend on the field strength), while it is directly controlled only by the magnetization parameter $k_{\rm pol}$ and a.

In the low-magnetization limit, when the magnetic energy $\mathcal{H}$ is smaller than the gravitational mass M ($\mathcal{H} \ll M$), the metric functions α and ψ depend weakly on the magnetic field strength, and one can safely assume for them the same values of the unmagnetized case. We have verified that the low-magnetization limit applies as long as the magnetic field at the centre is weaker than 10^{16} G (corresponding to a magnetic field at the surface smaller than a few 10^{15} G). For smaller values, non-linear variations are absent (changes in the results are well within the overall accuracy of the scheme), while they become evident at higher values. The reader is referred to Appendix A for a more detailed discussion on the strong field regime.

Interestingly, in this limit, it is possible to recast the current function $\mathcal{I}$ in a self-similar way, such that the resulting magnetic field configuration remains unchanged, modulo its strength. If J^ϕ is rescaled with a numerical factor η sending $k_{\rm pol} \mapsto \eta k_{\rm pol}$ and $a \mapsto \sqrt{\eta} a$, the solution of the GS equation itself is rescaled by the same numerical factor. The self-similar parameter can be thus defined in terms of the strength of the magnetic field as

$$\hat{a} = a\left(\frac{B_{\rm pole}}{10^{14}{\rm G}}\right)^{-1/2}, \tag{15}$$

where $B_{\rm pole}$ is the magnetic field at the pole, that we have decided to always normalize against 10^{14} G. Then the quantity $\hat{a}$ parametrizes the magnetic configurations, independently from the strength of the magnetic field. Notice that in PBD14, since the choice for the current function $\mathcal{I}$ in the TT case had a slightly different normalization, the role of self-similar parameter was assumed by a. Here, the new normalization improves the convergence of our scheme preventing the non-linear term from diverging at the highest value for a and λ. Moreover, it allows us to obtain also configurations with a complex magnetospheric field geometry (see Section 4). In this work, we will focus exclusively on the low-magnetization limit, considering for simplicity cases with $\zeta = 0$ or $\zeta = 1$.

3 NUMERICAL SETUP

The numerical scheme used to compute our models is fully described in Bucciantini & Del Zanna (2013) and in PBD14, to which the reader is referred for a more complete discussion. Here, we quickly summarize for convenience the main features and the few modifications introduced in this work.

The basic idea of the algorithm is to use an expansion in spherical harmonics to solve the non-linear Poisson-like equations, and reduce them to a set of ordinary second-order PDEs for each coefficient, that can be solved using a direct tridiagonal matrix inversion. In the weak-field limit, the metric and matter distributions are assumed to be the same as in the unmagnetized case, so that the we do not need to solve Einstein equations in the conformally flat condition (CFC) scheme and the problem is reduced to find the solution of the GS equation (7) alone, a non-linear vector Poisson equation for A_ϕ. Its solution is searched expanding $\tilde{A}_\phi$ by means of vector spherical harmonics (Barrera, Estevez & Giraldo 1985), that is

$$\tilde{A}_\phi(r,\theta) := \sum_{l=0}^{\infty}[C_l(r)Y_l'(\theta)]. \tag{16}$$

As already done in PBD14 the solution to the GS equation is searched over the entire numerical domain, which includes both the interior of the star and the surrounding magnetosphere, where the density, for numerical reasons, is set to a very small value (in principle it could be set to 0). With this approach, there is no need to match the exterior solution with the interior one (as it is usually done when the solution of the GS equation is separately computed over disconnected domains) and the smoothness of the solutions at the stellar surface is here automatically guaranteed avoiding the onset of spurious surface currents. The harmonic decomposition ensures the correct behaviour of the solution on the symmetry axis. At the centre of the star the radial coefficients $C_l(r)$ go to 0 with parity $(-1)^l$, while a correct asymptotic trend at larger radii (the outer boundary condition) is achieved by imposing $C_l(r) \propto r^{-(l+1)}$.

Being interested only in the study of the properties and geometry of the magnetic field, in all our models we assume the NS to be described by a simple polytropic EoS $p = K_a \rho^{\gamma_a}$ with an adiabatic index $\gamma_a = 2$ and a polytropic constant, expressed in geometrized units, $K_a = 110$. This is done in analogy with PBD14 and according to common choices in literature (Kiuchi & Yoshida 2008; Lander & Jones 2009). Our fiducial model has a central density $\rho_{\rm c} = 8.576 \times 10^{14}\,{\rm g\,cm^{-3}}$ a baryonic mass $M_0 = 1.680\,{\rm M}_\odot$,

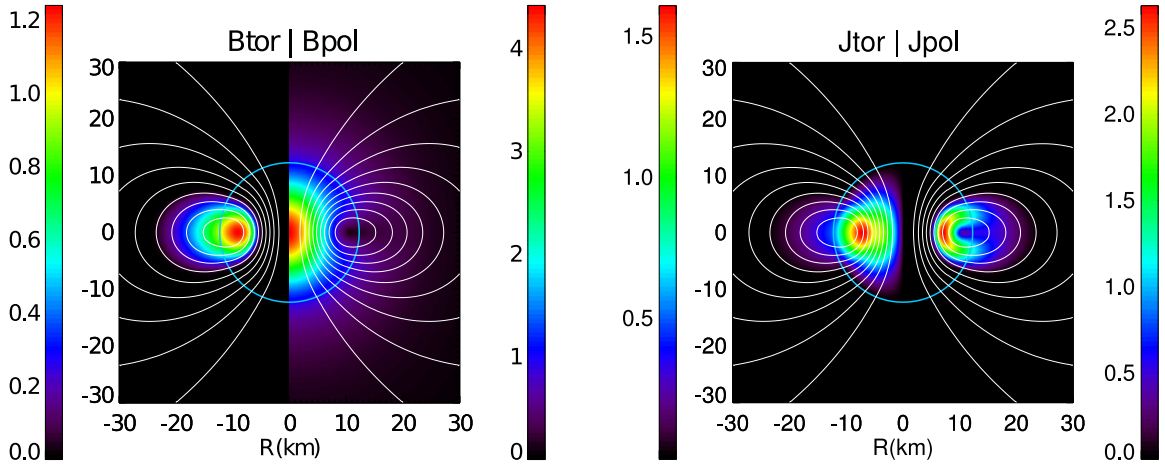

Figure 1. Left: strength of the toroidal (left half) and poloidal (right half) magnetic field in units of $B_{\rm pole}$. Contours represent magnetic field surfaces. Right: same as the left-hand panel for the toroidal (left half) and poloidal (right half) current density. The toroidal current density is expressed in units of $10^{18}\,{\rm G\,s^{-1}}$, the poloidal one in units of $10^{13}\,{\rm G\,s^{-1}}$. In both panels, the blue curves represent the surface of the star. This configuration has $\lambda = 2$ and $\hat{a} = 2.5$, corresponding the highest value for the magnetic energy ratio $\mathcal{H}_{\rm tor}/\mathcal{H} = 11.29 \times 10^{-2}$.

a gravitational mass $M = 1.551\,{\rm M}_\odot$, and a circumferential radius $R_{\rm circ} = 14.19\,{\rm km}$. For convenience the magnetic field at the pole is rescaled to $B_{\rm pole} = 10^{14}$ G (recall that results in the weak-field limit are actually independent from the field strength).

To explore the parameter space, we computed several equilibrium models for different values of the parameter λ (from $\lambda = 1$ to $\lambda = 8$) and for different values of the parameter $\hat{a}$.

The numerical solutions we present here are computed using 60 harmonics. Models with $\lambda < 4$ are computed over a uniform grid in spherical coordinates covering the range $r = [0, 40]$ and $\theta = [0, \pi]$ with 600 grid points in the radial direction and 400 points in the angular one. Models with $\lambda \geq 4$ have a twisted magnetosphere extending to larger radii. In order to retain the same accuracy in the inner region, and to reduce the computational time, we adopt a geometrically stretched grid in the range $r = [40, 150]$ defined on 200 grid points. The grid spacing Δr is chosen such that

$$\Delta r_i = (1 + 5.962 \times 10^{-3})\Delta r_{i-1}. \quad (17)$$

This permits to capture the entire twisted magnetosphere and to resolve the star always with the same accuracy, without resorting to huge numerical grids. The convergence tolerance for the iterative solution of GS equation has been fixed to $\sim 10^{-8}$, however, we have verified that the overall accuracy of our solution is $\lesssim 10^{-3}$ because of the discretizations errors.

4 RESULTS

In this section, we present the results of the GRMHD calculations. Since we focus on the low-magnetization limit, as discussed previously, global physical quantities such as the gravitational mass, the baryonic mass, and the circumferential radius do not change for the various sequences but remain equal to those of the fiducial model. Our discussion will concentrate only on the magnetic properties of the equilibrium configurations. All models are thus parametrized just in terms of $\hat{a}$, defining the magnetic field geometry, and λ, defining the extent of the magnetosphere. For convenience, magnetic field strengths are expressed in terms of their value at the pole $B_{\rm pole}$, that we arbitrarily assume to be $B_{\rm pole} = 10^{14}$ G.

In the following subsections, we will consider only configurations with $\zeta = 0$ and $\zeta = 1$. However, a detailed investigation about the effects of more different and general current distribution for both $\mathcal{I}$ and $\mathcal{M}$ can be found in Bucciantini et al. 2014.

4.1 Models with $\zeta = 0$

In Fig. 1, we show a typical example of an equilibrium model with a twisted magnetosphere. This specific configuration corresponds to $\lambda = 2$ and $\hat{a} = 2.5$. The poloidal magnetic field extends through the whole domain and reaches its maximum strength $B_{\rm pol}^{\rm max} = 4.422\,B_{\rm pole}$ at the centre of the star. The toroidal component of the magnetic field is, by construction, confined inside a closed region that extends in the radial direction from the interior of the star up to twice the stellar radius, and in latitude it is contained within a wedge about $\pm\pi/6$ around the equator. The maximum value of the toroidal magnetic field $B_{\rm pol}^{\rm max} = 1.256\,B_{\rm pole}$ is reached inside the star in correspondence to the neutral line where the poloidal magnetic field vanishes. The right-hand panel of Fig. 1 shows that the poloidal current density peaks inside the star, and extends smoothly outside the stellar surface along the magnetic field surfaces. The toroidal current, on the other hand, results from the sum of the linear current term in $\mathcal{M}$, $J^\phi = \rho h k_{\rm pol}$, fully confined within the star, and of the non-linear term in $\mathcal{I}$, that extends outside the star over the same region where the poloidal currents are confined.

The magnetospheric equilibria of the type shown in Fig. 1, and discussed above, are qualitatively similar to previous results (Mikic & Linker 1994; Viganò et al. 2011; Parfrey et al. 2013). However, in those cases the equilibria were obtained by the relaxation of an initially sheared dipolar configuration, while here we directly solve the GS equation. Such configurations, for a moderate shear of the magnetic footpoints, are expected to be stable. On the other hand, our approach based on the GS equation allows us to derive equilibrium models but, of course, it does not provide any hint about their stability. A more direct comparison can be made with Glampedakis et al. (2014), in spite of a different value $\zeta = 0.5$ employed, our solutions qualitatively agree with the one presented in more detail in the cited work.

In Fig. 2, we present sequences of models computed for various values of the parameters λ and $\hat{a}$. The main characteristics of those configurations are stated in Table 1. The results presented illustrate the key features and trends of the equilibrium configurations that we

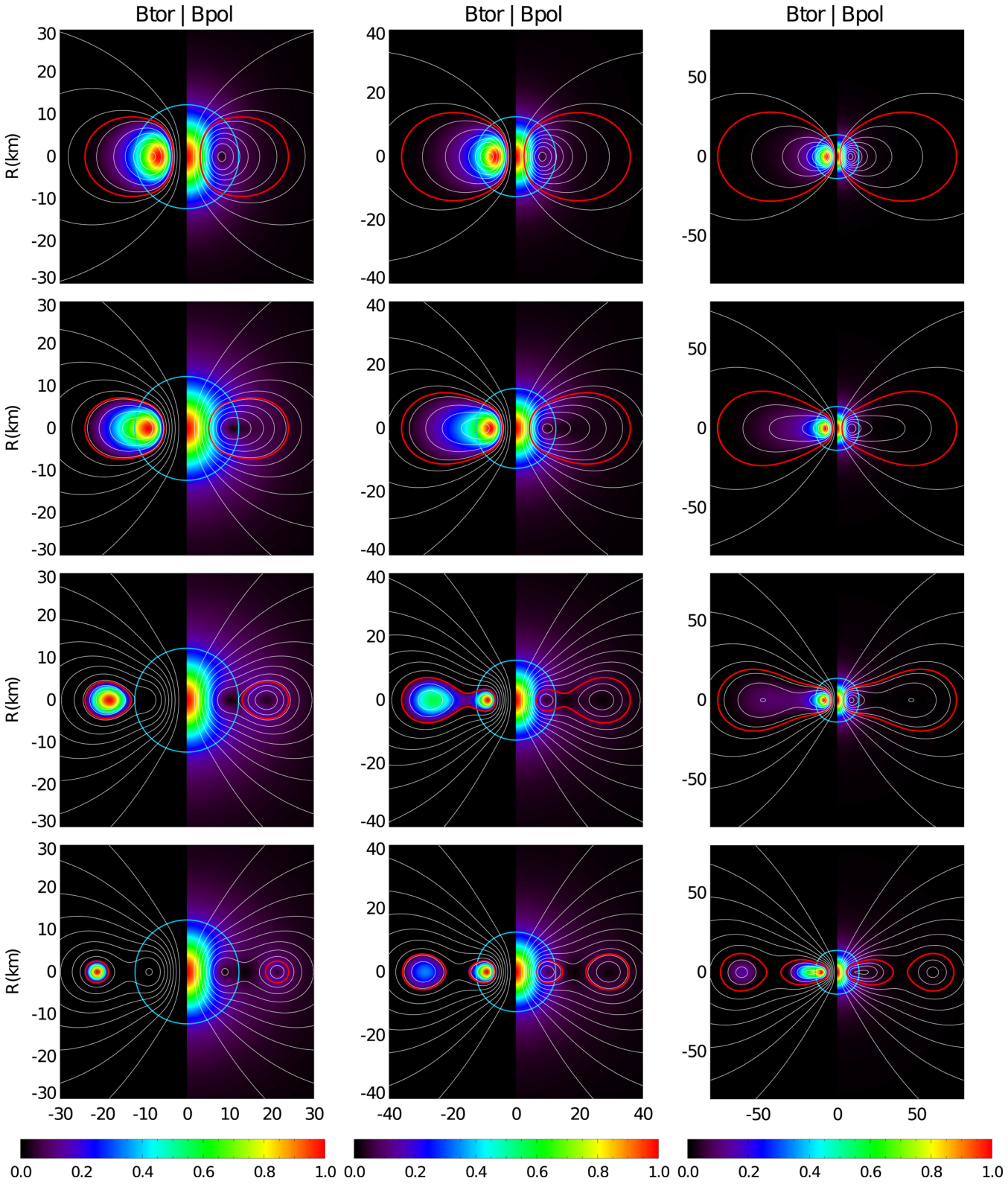

Figure 2. TT magnetosphere configurations: strength of the toroidal (left half of each panel) and poloidal (right half of each panel) magnetic field. The left-hand column shows models with $\lambda = 2$, the central column those with $\lambda = 3$, and the right-hand column those with $\lambda = 6$. Contours represent magnetic field surfaces. From top to bottom, each row corresponds to increasing values of $\hat{a}$, given in Table 1. For each panel, the colour code is normalized to the maximum value of the magnetic field components that are listed in Table 1. The blue line represents the surface of the star. The red line locates the boundary of the region where the toroidal component of the magnetic field is present.

Table 1. Values of the maximum strength of the toroidal and poloidal components of the magnetic field for the configuration shown in Fig. 2. Magnetic fields are expressed in unity of $B_{\rm pole}$.

λ	$\hat{a}$ (10^{-3})	$B_{\rm tor}^{\rm max}$	$B_{\rm pol}^{\rm max}$
2	0.4	0.359	5.629
	2.5	1.256	4.422
	5.6	0.938	4.576
	10	1.087	4.373
3	0.4	0.435	5.581
	1.5	1.004	4.577
	3.3	0.676	4.767
	4.2	1.170	4.618
6	0.4	0.491	5.352
	0.9	0.782	4.874
	1.3	0.822	4.842
	2.7	0.753	4.277

were able to obtain. For small values of the parameter $\hat{a}$ (first row of Fig. 2), all configurations share the same overall topology and a similar magnetic field distribution. The toroidal magnetic field fills a region that smoothly extends from the interior of the star to the maximum allowed radius λr_e. As it can be seen also from Fig. 3, the toroidal field component reaches, in this case, a maximum inside the star and then decreases monotonically in the magnetosphere. For small values of $\hat{a}$, the non-linear current terms associated with $\mathcal{I}$ outside the star are still too weak to significantly alter the magnetic field structure below the surface.

As the contribution of the non-linear currents become more important, with increasing $\hat{a}$, the toroidal field increases and its peak moves towards the stellar surface together with the poloidal neutral line. This is a typical behaviour of TT configurations, already observed in the case where the toroidal field is fully confined within the star (Ciolfi et al. 2009; Lander & Jones 2009; PBD14). As the toroidal magnetic field increases, the ratio of the magnetic energy associated with the toroidal field $\mathcal{H}_{\rm tor}$ with respect to the total magnetic energy $\mathcal{H}$ increases too, until it reaches a maximum. These maximal configurations are shown in the second row of Fig. 2. The structure and topology of the magnetic field is analogous to the small $\hat{a}$ cases (see also Fig. 3), however, the presence of stronger magnetospheric currents now affects the field geometry outside the star. While the outer magnetic field in the small $\hat{a}$ regime still resembles closely a dipole, this is no longer true for the maximal energy configurations, where magnetic surfaces appear to be stretched, especially for high values of λ. Note, moreover, that for higher λ, the configurations of maximum energy ratio are reached for smaller values of $\hat{a}$. This because the energy is an integrated quantity that depends not just on the strength of the currents but also on the volume they fill.

However, after the maximum value of $\mathcal{H}_{\rm tor}/\mathcal{H}$ has been reached, solutions react differently to a further increase of $\hat{a}$, depending on the value of the parameter λ. This can be seen in the third row in Fig 2 and in Fig. 3. In the case of $\lambda \leq 2$, the toroidal magnetic field migrates completely outside the star and the final outcome strictly resembles that of the TT case with $\lambda = 1$ discussed in PBD14: the toroidal magnetic field strength grows but its support progressively shrinks towards the maximum allowed radius. Here, the toroidal magnetic field shows a single maximum. On the other hand, for $\lambda \geq 3$, as the neutral line approaches the stellar surface, a second peak in the strength of the toroidal magnetic field develops. This second peak moves with increasing $\hat{a}$ at larger radii in the magnetosphere, while the first peak remains inside the star, approximatively at the same position, independently of $\hat{a}$. The formation of a second peak indicates a topological change in the structure of the magnetic field, where an X-point arises, usually in the vicinity of the stellar surface, and where there are magnetic regions (surfaces) in the magnetosphere disconnected from the star. A further increase in the value of $\hat{a}$ leads to solutions that show two completely disconnected magnetic regions, one inside the star, and the other outside (see the fourth row of Fig. 2). Note also that the maximum value of the strength of the toroidal magnetic field $B_{\rm tor}^{\rm max}$ does not grow monotonically with $\hat{a}$.

These types of equilibria, with disconnected magnetic regions, are likely to be highly unstable. Indeed, those kind of equilibria resemble the solutions find in time-dependent numerical simulation by Mikic & Linker (1994) in the context of magnetic field arcades in the solar corona, and *plasmoid* formation. Indeed, our disconnected regions in the NS magnetosphere could be seen as the equivalent of the plasmoids in the solar case.

While a full 3D study of the stability and/or evolution, of the various topological configurations, is beyond the scope of this paper, it is possible to roughly evaluate the magnetospheric conditions, in relation to known stability criteria. We need also to recall here that the physical regime, to which our models apply, is typical of the late phases of the proto-NS evolution, when a crust begins to form.

In all the obtained configurations, the energy of the external toroidal magnetic field is, at most, 25 per cent of the total magnetic energy in the magnetosphere which is, thus, dominated by

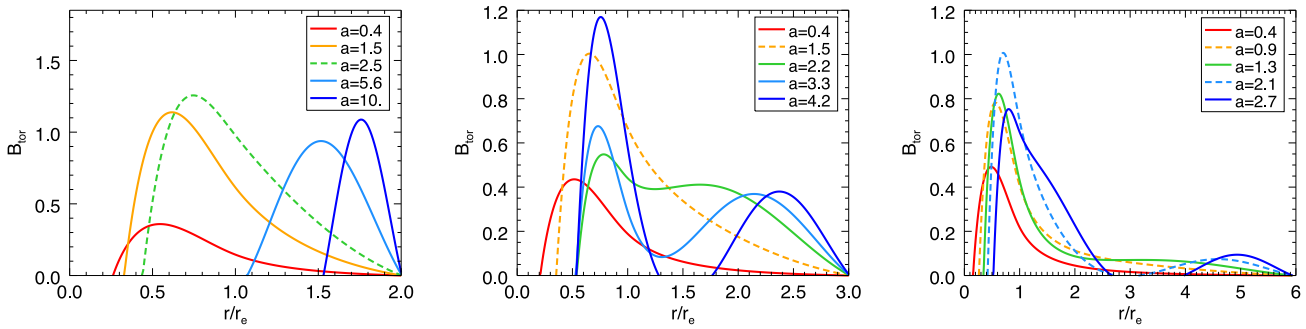

Figure 3. Profiles of the toroidal magnetic field strength (in units of $B_{\rm pole}$) for selected models ($\hat{a}$ is expressed in units of 10^{-3}) along the equilibrium sequences with $\lambda = 2$ (left), $\lambda = 3$ (centre) and $\lambda = 6$ (right). The dashed lines represent models where the value of $\mathcal{H}_{\rm tor}/\mathcal{H}$ reaches a maximum.

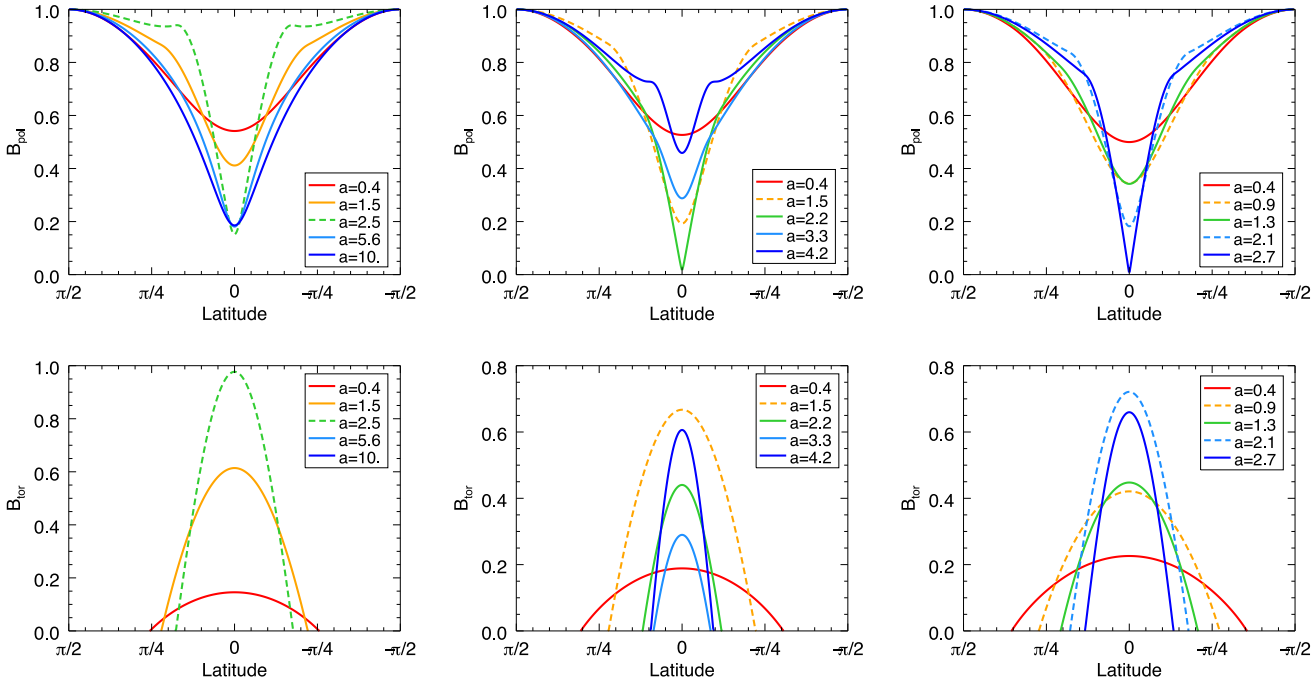

Figure 4. Profiles of the strength (expressed in units of $B_{\rm pole}$) of the poloidal (top panel) and toroidal (bottom panel) magnetic field on the stellar surface for selected models ($\hat{a}$ is expressed in units of 10^{-3}) along the equilibrium sequences with $\lambda = 2$ (left), $\lambda = 3$ (centre) and $\lambda = 6$ (right). The dashed lines represent models where the value of $\mathcal{H}_{\rm tor}/\mathcal{H}$ reaches a maximum.

the poloidal field. It is important, at this point, to distinguish between those configurations, where all field lines thread the crust, and those with disconnected region. In the first case, if the poloidal component can be stabilized by the crust (which can be the case for weak fields $\lesssim 10^{14}$G), then it is unlikely that the toroidal one, being subdominant, could drive major changes in the magnetospheric structure. It is possible to compare our results to those by Parfrey et al. (2013), where a study of the magnetospheric stability was done using a time dependent shearing algorithm. We find in our models (those with no disconnected regions) that the twist amplitude, defined as the azimuthal angular displacement of the magnetospheric footpoints, does not exceed 2 rad. This value is below the critical value of 3.65 rad estimated in Parfrey et al. (2013) as a stability limit for the magnetosphere.

In the other cases, when a disconnected toroidal current loop develops in the magnetosphere around the neutral line, since some of the magnetic field lines do not cross the crust, the twist amplitude is not an indicative parameter for the stability, and one cannot invoke for this disconnected region a stabilizing effect of the crust. However, the stability of this flux rope, can be determined from the Kruskal–Shafranov condition for the development of kink instability (Shafranov 1956; Kruskal & Tuck 1958). The value of the safety factor is $\sim$1 for detached flux ropes contained inside $1.3r_{\rm e}$ (suggesting a possible marginal stability) but rapidly drops to lower values as this disconnected region extends further out from the star. Therefore, small disconnected magnetospheric regions just above the surface of the star appear more stable than inflated ones at larger distance.

The reason why the GS equation, for large $\hat{a}$, admits solutions with multiple peaks can be easily understood. The solution of the GS equation can be seen as an eigenvalue problem for a second-order non-linear PDE. For small values of $\hat{a}$, the source terms in the currents are dominated by $\mathcal{M}$: they are fully confined within the star and have a single peak. Thus, the solution reflects the properties of the source, and only single-peak eigenmodes are selected. However, for higher values of $\hat{a}$, non-linear terms dominate, and other possible eigenmodes can be selected. Eigenmodes that for a second-order non-linear PDE, in principle will admit multiple radial nodes (this is the reason why two peaks develop). Indeed, as can be seen from Figs 2 and 3, there is some hint that the more extreme case at $\lambda = 6$ might develop into a third peak. Unfortunately, we could not investigate higher values of $\hat{a}$ because the convergence of the GS solver becomes highly oscillatory, and ultimately fails.

In Fig. 4, we show the profiles of the poloidal and toroidal components of the magnetic field along the stellar surface. In the small $\hat{a}$ regime, the poloidal field at the surface is essentially dipolar. The toroidal magnetic field extends over a region $\pm 45^\circ$ in latitude around the equator, slightly bigger for larger values of λ. Trends are different depending if the structure evolves to a single peak or double peak. For $\lambda \leq 2$ (single peak), as $\hat{a}$ increases, the magnetic field becomes slightly higher in the polar region but decreases substantially at the equator. As the peak moves outwards, so does the poloidal neutral line (where the poloidal field vanishes). This is the reason why the equatorial field drops. The magnetic field at the surface becomes closer to a split monopole: the curvature of magnetic field surfaces diminishes, the radial component becomes more uniform, except very close to the equator. The portion of the surface where $B_{\rm tor} \neq 0$ instead shrinks, and vanishes completely once the twisted region gets out of the star. In Fig. 5, we show the harmonic content C_l/C_1 of the surface magnetic field for different models, in the case $\lambda = 2$. As expected the dipole term is always the dominant one. Multipole terms become more important in correspondence to configurations with the higher $\mathcal{H}_{\rm tor}/\mathcal{H}$, when the toroidal field is stronger and the neutral line is located just underneath the stellar surface. Finally, as the twisted magnetospheric torus moves away from the star, the multipolar content of the surface field drops.

For higher values of $\lambda \geq 3$, the appearance of multiple peaks and disconnected magnetic regions leads to a more complex behaviour

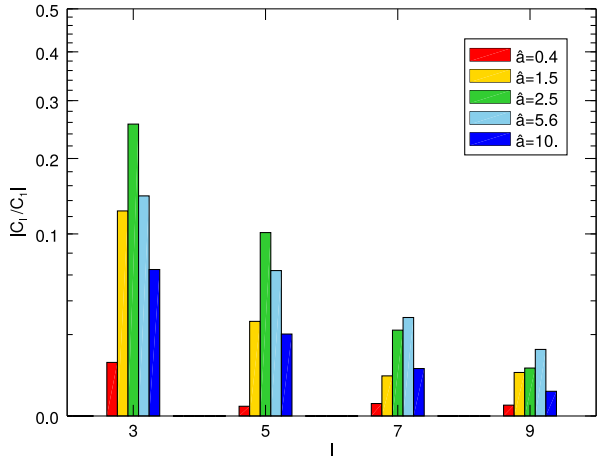

Figure 5. Harmonic content C_l/C_1 of the magnetic field at the surface of the star in the case $\lambda = 2$ for the selected models shown in the upper left-hand panel of Fig. 4.

of the magnetic field at the surface. In the polar regions at high latitude $>45^\circ$, the value of the poloidal field does not change much with increasing $\hat{a}$. As $\hat{a}$ increases the value of the poloidal field at the equator drops, but in this case this is not due to the neutral line moving outwards, but because an X-point forms in the vicinity of the surface. Indeed, as can be seen in Figs 4 and 2, in the $\lambda = 3$ case the values of $\hat{a}$ for which the poloidal field vanishes at the equator is the same at which a second peak forms. For higher values of $\hat{a}$, the equatorial poloidal field rises again. The portion of the surface where $B_{\rm tor} \neq 0$ shrinks again, though for these cases it never vanishes completely. In all cases, we find that the strength of the toroidal component of the magnetic field at the surface tends to grow becoming comparable to, or even exceeding, the strength of the poloidal one. Another parameter that is useful to show is the angle between the magnetic field and the meridional plane, to which we refer as twist angle $\Delta\varphi$. For convenience, it can be defined as the complementary of the angle that the magnetic field forms with respect to the azimuthal direction

$$\Delta\varphi = \arcsin\left[\left(B_\phi B^\phi / B_i B^i\right)^{1/2}\right]. \tag{18}$$

The value of $\Delta\varphi$ ranges from 0 to $\pi/2$, assuming the latter when the magnetic field is purely azimuthal, and 0 when the magnetic field lies in the meridional plane. In Fig. 6, we show this angle, measured at the equator, as a function of radial distance r. Since our models are not rotating, all the magnetic field lines are eventually closed. The location where $\Delta\varphi = \pi/2$ corresponds to the location of either the neutral line (O-point) or the X-point, where the poloidal component of the magnetic field vanishes. For cases with $\lambda \leq 2$, the profile of $\Delta\varphi$ shows a unique peak where the θ component of the poloidal field reverses sign in the twisted region. Again we see that at higher values of $\hat{a}$ the toroidal field is completely outside the star.

As expected, in the case $\lambda \geq 3$, the behaviour is more complex. For the smallest value of $\hat{a}$, the trend of $\Delta\varphi$ resembles that of the analogous configuration at $\lambda = 2$: the twist is prominent in the vicinity of the neutral line and extends outside the star remaining well below $\sim\pi/4$. Moving at higher $\hat{a}$, the presence of two peaks in the toroidal magnetic field strength inside the twisted region means that $\Delta\varphi$ reaches $\pi/2$ in three locations. In particular, the first and the third of those locations are always associated with O-points, the second one with an X-point. At the higher value of $\hat{a}$, the formation of two detached twisted regions is also evident. In these cases, however, the trend of $\Delta\varphi$ reveals only the position of the two O-point because the ϕ component of the magnetic field vanishes in correspondence with the X-point. Here, we note that in the most extreme case at $\lambda = 6$ the trend of $\Delta\varphi$ strengthen the hypothesis concerning the development of a third peak in the toroidal magnetic

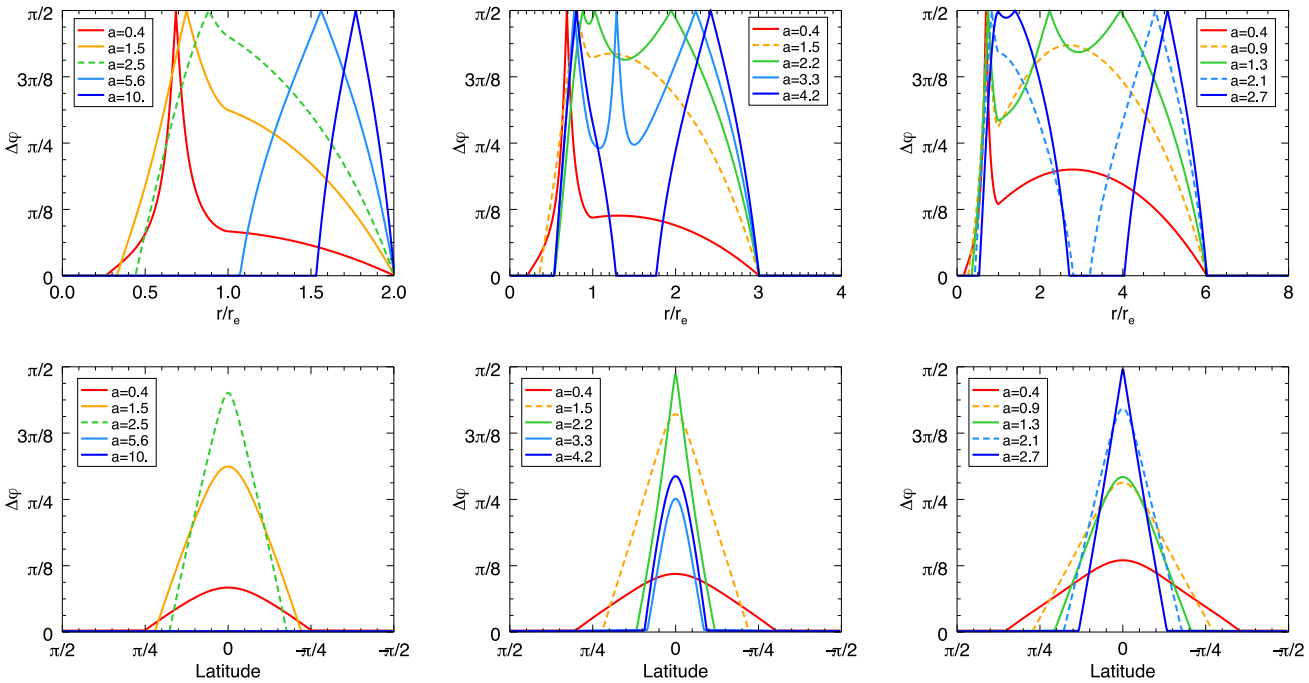

Figure 6. Profiles of the twist angle $\Delta\varphi$ at the equator as a function of distance (normalized to the stellar radius r_e) (upper panels), and as a function of latitude on the stellar surface (bottom panels), for selected models ($\hat{a}$ is expressed in units of 10^{-3}) along the equilibrium sequences with $\lambda = 2$ (left), $\lambda = 3$ (centre) and $\lambda = 6$ (right). The dashed lines represent models with maximum value of $\mathcal{H}_{\rm tor}/\mathcal{H}$ along the same sequences.

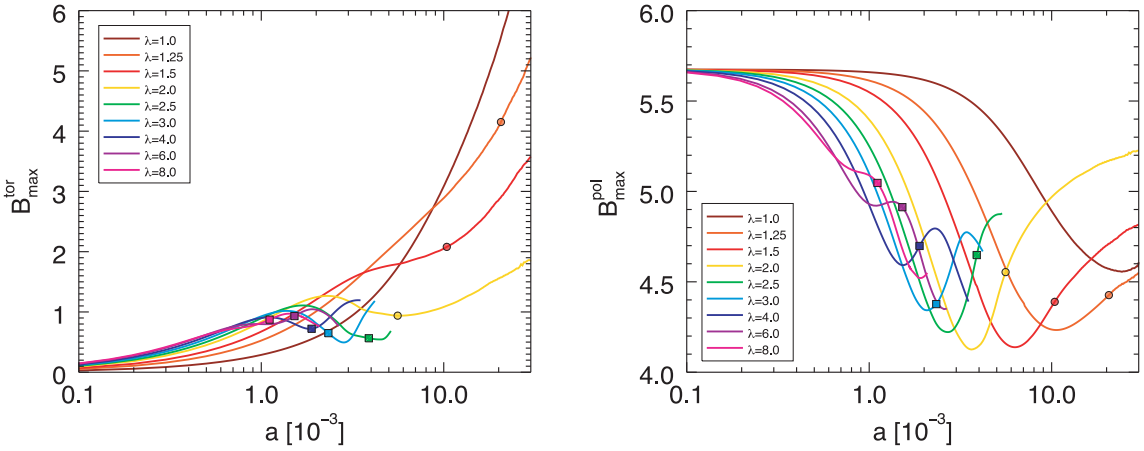

Figure 7. Maximum value of the toroidal (left) poloidal (right) magnetic field along equilibrium sequences with different values of λ. Dots indicate configurations where the toroidal magnetic field component is completely outside the star. The squares indicate configurations which show two maxima of the toroidal magnetic field.

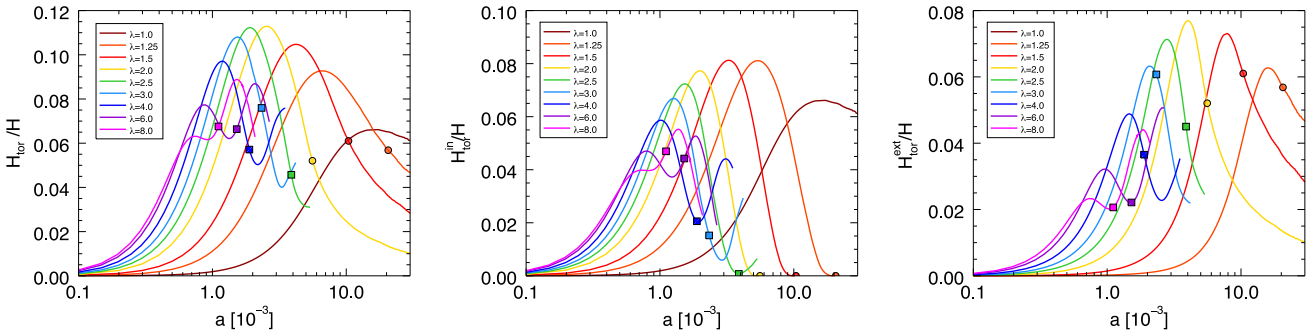

Figure 8. Profiles of the ratio of total magnetic energy of the toroidal component $\mathcal{H}_{\rm tor}$, external one $\mathcal{H}^{\rm ext}_{\rm tor}$ and internal one $\mathcal{H}^{\rm in}_{\rm tor}$, with respect to the total magnetic energy $\mathcal{H}$. The curves show sequences as a function of $\hat{a}$ for various values of λ. The dots and squares as in Fig. 7.

field strength. Indeed, the second peak in $\Delta\varphi$ corresponds to an O-point and an unresolved X-point.

The bottom row of Fig. 6 displays the profile of $\Delta\varphi$ along the stellar surface. As pointed out before, in the limit of small $\hat{a}$ the twist at the surface increases. However, for higher values of $\hat{a}$ the trend is not uniform, depending on the formation of a second peak, and the related location of the X-point.

In Fig. 7, we plot the maximum value of the strength of the toroidal magnetic field $B^{\rm max}_{\rm tor}$, and the poloidal one $B^{\rm max}_{\rm pol}$, for different values of λ, as a function of $\hat{a}$. In all our models, the poloidal field reaches its maximum at the centre. Initially, in the small $\hat{a}$ regime, $B^{\rm max}_{\rm tor}$ grows, while $B^{\rm max}_{\rm pol}$ decreases. This happens because the strength of the magnetic field at the pole is always kept fixed in all models. As one enhances the contribution to the total current by increasing $\mathcal{I}$, one must decrease the contribution from $\mathcal{M}$, causing a drop in the strength of the field at the centre of the star. This effect depends also on the location of the current, as this term moves to larger radii the poloidal field begins to grow again. Configurations with $\lambda \geq 3$ show several inversions of this trend, which again are a manifestation of the change in the field topology.

All the equilibrium models we obtain are energetically dominated by the poloidal magnetic field. This was found to apply also for models where the twist is fully confined with the star (Ciolfi et al. 2009; Lander & Jones 2009; PBD14). In Fig. 8, we show the same equilibrium sequences in terms of the ratio of magnetic energy of the toroidal magnetic field $\mathcal{H}_{\rm tor}$ over the total magnetic energy $\mathcal{H}$. Generally, the magnetic energy ratio initially grows with $\hat{a}$ reaching a first maximum that corresponds to a configuration still characterized by a single peak (see the first rows of Fig. 1). Again the trend for higher values of $\hat{a}$ depends on the value of λ. While sequences with $\lambda \leq 2$ show a decreasing monotonic trend, sequences with $\lambda \geq 3$ reach a minimum and then the magnetic energy ratio begin to grow again. For configurations with $\lambda \gtrsim 6$, we could reach a second local maximum. It is possible in principle that other maxima and minima could be reaches at higher values of $\hat{a}$, but we could not compute those models. The magnetic energy is an integrated quantity, as such it also depends on the size of the twisted region. The formation of an X-point, followed by the formation of two detached magnetic twisted domains, is associated with a decrease of the net volume taken by the toroidal field, and to the drop of $\mathcal{H}_{\rm tor}$ after the first maximum.

In Fig. 8, we also compare the toroidal magnetic energy confined inside $\mathcal{H}^{\rm in}_{\rm tor}$ and outside $\mathcal{H}^{\rm ext}_{\rm tor}$ the star. The two are in general comparable except for cases with $\lambda \leq 2$ where the interior toroidal field vanishes at high $\hat{a}$. Note also that the ratio $\mathcal{H}_{\rm tor}/\mathcal{H}$ is at most 8–10 per cent. The net poloidal and toroidal currents follow a similar behaviour.

Finally, in Fig. 9, we show the variation of the magnetic dipole moment μ as a function of $\hat{a}$. We see that the magnetic dipole, for fixed values of $\hat{a}$, grows with λ. This is because the total integrated toroidal current, defined as

$$\mathcal{J} = \int \sqrt{J^{\phi} J_{\phi}}\, \psi^6 r^2 \sin\theta \mathrm{d}r\mathrm{d}\theta\mathrm{d}\phi \qquad (19)$$

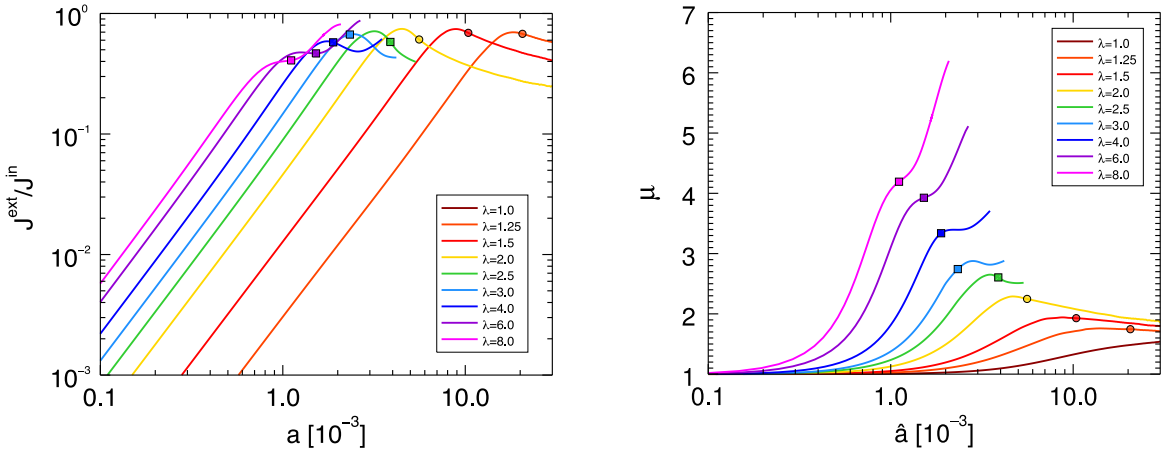

Figure 9. Left-hand panel: ratio between the toroidal current density outside the star $\mathcal{J}^{\rm ext}$ and the toroidal current density inside $\mathcal{J}^{\rm in}$, as a function of $\hat{a}$ along equilibrium sequences with different value of λ. Right: magnetic dipole moment μ along the same sequences expressed in units of the magnetic dipole moment of the fiducial configuration $\mu = 1.114 \times 10^{32}\,{\rm erg\,G^{-1}}$. The dots and squares as in Fig. 7.

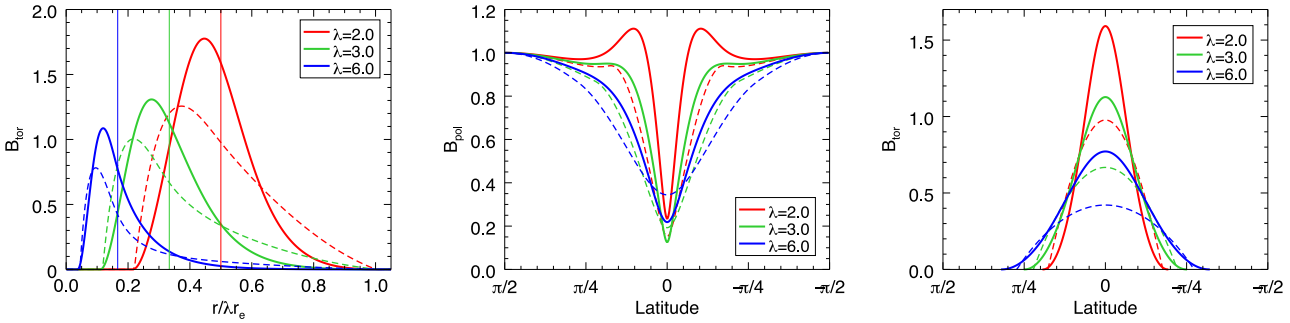

Figure 10. The left-hand panel shows the profile of the toroidal magnetic field strength (in units of $B_{\rm pole}$) for the configuration with the first maximum value of the magnetic energy ratio $\mathcal{H}_{\rm tor}/\mathcal{H}$ along sequences with fixed λ =2, 3 and 6. The solid lines refer to configurations with $\zeta = 1$, while dashed ones refer to the equivalent configurations with $\zeta = 0$. The thin vertical lines indicate the location of the stellar surface for each λ. The remaining panels show, for the same configurations, the profile of the magnetic field strength, evaluated at the surface of the star, for the poloidal (centre) and the toroidal component (right) as a function of latitude.

is bigger for larger magnetospheres with higher values of λ. Very interestingly, for large values of λ the net magnetic dipole moment can be even four to five times higher, given the same strength of the field at the pole. External currents contribute to the net dipole without affecting too much the strength of the magnetic field at the surface. This is a known property of twisted magnetospheres (Thompson et al. 2002).

For all the configurations computed here, the internal linear current $\mathcal{J}^{\rm in}$ is always greater than the external one $\mathcal{J}^{\rm ext}$, reaching similar values only for configuration where the energy ratio reaches a maximum. At first, as expected, the external current, due only to the term $\mathcal{I}$, grows linearly with $\hat{a}^2$, while the internal one dominated by $\mathcal{M}$ remains more or less constant. For higher values of $\hat{a}$, the ratio decreases exactly for the same volumetric effect that was discussed for the trend of $\mathcal{H}_{\rm tor}/\mathcal{H}$.

4.2 Models with $\zeta = 1$

The toroidal magnetization index ζ controls the shape of the current distribution inside the torus-like region of the twisted field. With respect to the $\zeta = 0$ case, choosing higher value for ζ entails stronger currents mostly concentrated in the proximity of the neutral line. In this section, we will consider the $\zeta = 1$ case in order to show which are the possible qualitative and quantitative differences that can arise if a different value of ζ is chosen.

In order to compare the results with those at $\zeta = 0$, let us focus to those configurations where $\mathcal{H}_{\rm tor}/\mathcal{H}$ is maximal. In Fig. 10, we show the strength of the magnetic field, both at the surface and along the equator, in the cases λ =2, 3 and 6, compared with that of the equivalent configurations at $\zeta = 0$. In the $\zeta = 1$ case, the toroidal magnetic field reaches higher values than in the $\zeta = 0$ case. However, even though the geometry and shape of the twisted region remains almost the same, the distribution of the magnetic field is more concentrated around the peak and the magnetic field decays more rapidly to zero in the magnetosphere.

Looking at the distribution of the poloidal and toroidal field at the surface of the star (central and right-hand panel in Fig. 10) it is evident that the multipolar terms of the magnetic field become more important in the $\zeta = 1$ cases: while the strength of the poloidal magnetic field at the equator decreases marginally, it increases in the neighbouring region where it can also exceed the value of $B_{\rm pole}$ within a wedge of about $\pm\pi/4$ around the equator. While the portion of the surface where $B_{\rm tor} \neq 0$ remains approximatively the same the toroidal field is now more concentrated around the equator where its strength can be a factor of ∼2 higher than for $\zeta = 0$.

The effects of the new current distribution on the twist angle $\Delta\varphi$ are shown in Fig. 11, where we plot the trend of $\Delta\phi$ for the same

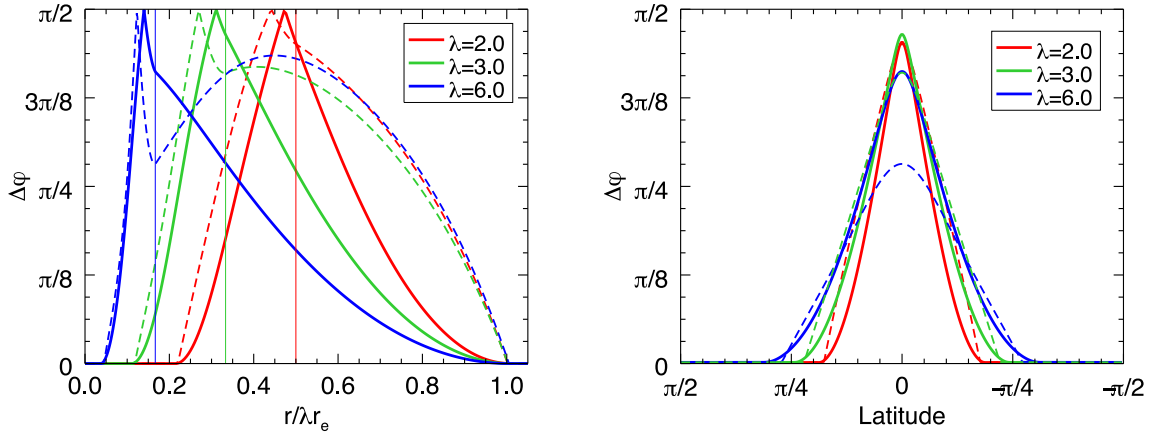

Figure 11. Profiles of the twist angle $\Delta\varphi$ in the magnetosphere (left) and at the stellar surface (right) for the same equilibrium configurations whose magnetic field profiles have been shown in Fig. 10. The solid lines (dashed lines) refer to configurations with $\zeta = 1$ ($\zeta = 0$).

equilibria discussed above. While the growth of the surface $\Delta\phi$ is a direct consequence of the stronger toroidal field obtained for the $\zeta = 1$ configurations, the analysis of trends in the magnetosphere deserve more attention. In fact, even though the toroidal field in the new configurations is stronger in the proximity of the stellar surface, the twist angle in the magnetosphere decreases monotonically and it is highly suppressed with respect to that obtained in the $\zeta = 0$ models. This is due, on the one hand, to the fact that $B_{\rm tor}$ goes more rapidly to zero in the magnetosphere but, on the other hand, also to the presence of a stronger equatorial poloidal field in the vicinity of the star.

The structure of the magnetic field is however only slightly affected by the value of the magnetic index ζ. This is also evident from Fig. 12, where we plot the profile of both the magnetic energy ratio $\mathcal{H}_{\rm tor}/\mathcal{H}$ and the current ratio $\mathcal{J}^{\rm ext}/\mathcal{J}^{\rm in}$ as a function of $\hat{a}$ for the various sequences. The trends strictly reflect those obtained in the $\zeta = 0$ case (see Figs 8 and 9) and it is interesting to notice that sequences with equal λ behave, from the point of view of the field topology, in the same way: for sequences with $\lambda \lesssim 2$ the twisted region moves outside the star; for sequences with $\lambda \gtrsim 2.5$ the configuration at higher $\hat{a}$ are characterized by a more complex topology and part of the toroidal field remain always confined in the star. Also a more quantitative comparison shows little differences. In the $\zeta = 1$ case, the maximum allowed $\mathcal{H}_{\rm tor}/\mathcal{H}$ is lower if $\lambda \lesssim 2.5$ and higher if $\lambda > 2.5$. The major differences regard the sequences with $\lambda = 6$ and 8 where the higher value of $B_{\rm tor}$ and a more regular topology of the solution (i.e. there is no formation of an X-point) allow us to reach higher value for the magnetic energy ratio. Finally, in both cases, when $\mathcal{J}^{\rm ext} \sim 0.7\mathcal{J}^{\rm in}$, the system self-regulates inducing a change in the topology of the distribution of the magnetic field and the associated external current.

5 CONCLUSIONS

There is an ever increasing amount of evidence that magnetars have a strongly twisted magnetosphere, and that it is this twist more than the strength of the field itself that defines their phenomenology, and isolate them as a separate class of NS. Investigating how this twisted magnetosphere is arranged, and what could be its equilibrium structure, is thus an important step for a more realistic description of these astrophysical sources.

We have computed numerically, for the first time, equilibrium models of general relativistic magnetized NSs with twisted magnetospheres, allowing for electric currents extending smoothly from the interior of the star to the exterior. Our work extends a recent study by Glampedakis et al. (2012) in the Newtonian regime.

Our models represent a straightforward generalization of typical TT configurations, where the twist is allowed to extend also outside

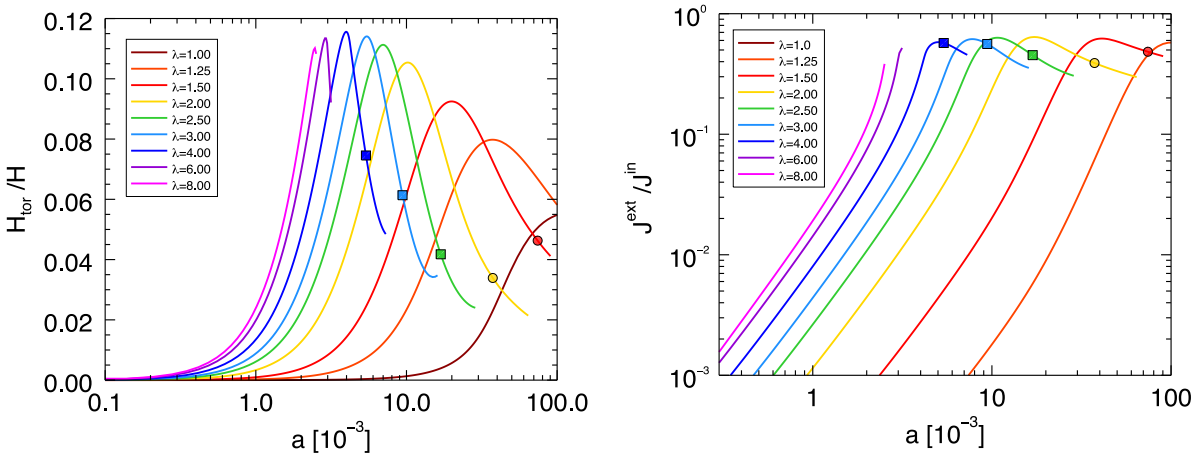

Figure 12. Profiles of the toroidal energy ratio $\mathcal{H}_{\rm tor}/\mathcal{H}$ (left) and of the current ratio $\mathcal{J}^{\rm ext}/\mathcal{J}^{\rm in}$ as a function of $\hat{a}$ along equilibrium sequences with constant λ. The dots and squares as in Fig. 7.

the NS. In particular, we have focused on the low-magnetization limit, since this limit is appropriate for real physical system such as AXPs and SGRs. In this case, the morphology of the magnetic field can be fully parametrized in terms of a single quantity $\hat{a}$, independently of the strength of the magnetic field. We have shown that the extent of the magnetosphere (our parameter λ) plays an important role and defines the possible existence of different topological classes of solutions.

In the low $\hat{a}$ regime, when the non-linear current terms are weak, the magnetic field lines are inflated outward by the toroidal magnetic field pressure and the twist of the field lines extends also to higher latitude. The result is a single magnetically connected region. As $\hat{a}$ increases, the effects of the non-linearity of the equation start to arise. This not only reduces the twist of the near-surface magnetic field but also leads to the formation of a disconnected magnetic island, reminiscent of the so-called plasmoids often found in simulations of the solar corona. This regime and these topologies are very likely to be unstable.

In this work, we focused on configurations with a magnetospheric confined twist exploring the effects of different choices for the strength and shape of the twist. Even though, as pointed out in Beloborodov (2011), the observations of shrinking hotspots on magnetar transient seem to suggest that the twist is more probably located near the pole, similar magnetospheric geometries have been recently used to model SGR giant flare as flux rope eruption (Huang & Yu 2014a,b).

Our approach to NS magnetospheric equilibrium has allowed us to obtain complex magnetic field morphologies. However, apart from a rough estimate based on known criteria, it is difficult to establish their stability, especially with respect to non-azimuthal perturbations. Moreover, since we treat the magnetosphere as force-free plasma, the physical regime to which our models apply, is characteristic of the late phases of a proto-NS, when a crust begins to form. Therefore, a meaningful modellization of the evolution of the system cannot disregard the important stabilizing role played by the crust. This is just indicative of the great complexity of the physic involved, and correspondingly of the extreme difficulties in the realistic modelling of NS structure.

ACKNOWLEDGEMENTS

This work has been supported by a EU FP7-CIG grant issued to the NSMAG project (PI: NB), and by the INFN TEONGRAV initiative (local PI: LDZ).

REFERENCES

Barrera R. G., Estevez G. A., Giraldo J., 1985, Eur. J. Phys., 6, 287
Beloborodov A. M., 2011, in Torres D. F., Rea N., eds, High-Energy Emission from Pulsars and their Systems, Springer-Verlag, Berlin, p. 299
Beloborodov A. M., Thompson C., 2007, Ap&SS, 308, 631
Bocquet M., Bonazzola S., Gourgoulhon E., Novak J., 1995, A&A, 301, 757
Bonanno A., Rezzolla L., Urpin V., 2003, A&A, 410, L33
Bonazzola S., Gourgoulhon E., 1996, A&A, 312, 675
Braithwaite J., 2009, MNRAS, 397, 763
Braithwaite J., Nordlund Å., 2006, A&A, 450, 1077
Braithwaite J., Spruit H. C., 2006, A&A, 450, 1097
Bucciantini N., Del Zanna L., 2011, A&A, 528, A101
Bucciantini N., Del Zanna L., 2013, MNRAS, 428, 71
Bucciantini N., Pili A. G., Del Zanna L., 2014, MNRAS, preprint (arXiv:1412.5347)
Bucciantini N., Quataert E., Metzger B. D., Thompson T. A., Arons J., Del Zanna L., 2009, MNRAS, 396, 2038
Bucciantini N., Metzger B. D., Thompson T. A., Quataert E., 2012, MNRAS, 419, 1537
Burrows A., Dessart L., Livne E., Ott C. D., Murphy J., 2007, ApJ, 664, 416
Carter B., 1970, Commun. Math. Phys., 17, 233
Carter B., 1973, in De Witt C., De Witt B. S., eds, Black Holes (Les Houches 1972), Gordon and Breach, New York, p. 57
Chandrasekhar S., Fermi E., 1953, ApJ, 118, 116
Ciolfi R., Rezzolla L., 2012, ApJ, 760, 1
Ciolfi R., Rezzolla L., 2013, MNRAS, 435, L43
Ciolfi R., Ferrari V., Gualtieri L., Pons J. A., 2009, MNRAS, 397, 913
Ciolfi R., Ferrari V., Gualtieri L., 2010, MNRAS, 406, 2540
Contopoulos I., Kazanas D., Fendt C., 1999, ApJ, 511, 351
Contopoulos I., Kalapotharakos C., Kazanas D., 2014, ApJ, 781, 46
Cordero-Carrión I., Cerdá-Durán P., Dimmelmeier H., Jaramillo J. L., Novak J., Gourgoulhon E., 2009, Phys. Rev. D, 79, 024017
Duncan R. C., Thompson C., 1992, ApJ, 392, L9
Fernández R., Thompson C., 2007, ApJ, 660, 615
Frieben J., Rezzolla L., 2012, MNRAS, 427, 3406
Fujisawa K., Yoshida S., Eriguchi Y., 2012, MNRAS, 422, 434
Glampedakis K., Andersson N., Lander S. K., 2012, MNRAS, 420, 1263
Glampedakis K., Lander S. K., Andersson N., 2014, MNRAS, 437, 2
Goldreich P., Julian W. H., 1969, ApJ, 157, 869
Gourgoulhon E., Markakis C., Ury u K., Eriguchi Y., 2011, Phys. Rev. D, 83, 104007
Gourgouliatos K. N., Cumming A., Reisenegger A., Armaza C., Lyutikov M., Valdivia J. A., 2013, MNRAS, 434, 2480
Huang L., Yu C., 2014a, ApJ, 784, 168
Huang L., Yu C., 2014b, ApJ, 796, 3
Kalapotharakos C., Contopoulos I., 2009, A&A, 496, 495
Kiuchi K., Yoshida S., 2008, Phys. Rev. D, 78, 044045
Kouveliotou C. et al., 1999, ApJ, 510, L115
Kruskal M., Tuck J. L., 1958, R. Soc. Lond. Proc. Ser. A, 245, 222
Kuiper L., Hermsen W., den Hartog P. R., Collmar W., 2006, ApJ, 645, 556
Lander S. K., Jones D. I., 2009, MNRAS, 395, 2162
Lander S. K., Jones D. I., 2011a, MNRAS, 412, 1394
Lander S. K., Jones D. I., 2011b, MNRAS, 412, 1730
Lasky P. D., Melatos A., 2013, Phys. Rev. D, 88, 103005
Low B. C., Lou Y. Q., 1990, ApJ, 352, 343
Lyutikov M., Gavriil F. P., 2006, MNRAS, 368, 690
Makishima K., Enoto T., Hiraga J. S., Nakano T., Nakazawa K., Sakurai S., Sasano M., Murakami H., 2014, Phys. Rev. Lett., 112, 171102
Mastrano A., Melatos A., Reisenegger A., Akgün T., 2011, MNRAS, 417, 2288
Mereghetti S., 2008, A&AR, 15, 225
Metzger B. D., Giannios D., Thompson T. A., Bucciantini N., Quataert E., 2011, MNRAS, 413, 2031
Mikic Z., Linker J. A., 1994, ApJ, 430, 898
Nobili L., Turolla R., Zane S., 2008, MNRAS, 389, 989
Parfrey K., Beloborodov A. M., Hui L., 2013, ApJ, 774, 92
Pavan L., Turolla R., Zane S., Nobili L., 2009, MNRAS, 395, 753
Perna R., Gotthelf E. V., 2008, ApJ, 681, 522
Philippov A., Tchekhovskoy A., Li J. G., 2014, MNRAS, 441, 1879
Pili A. G., Bucciantini N., Del Zanna L., 2014, MNRAS, 439, 3541 (PBD14)
Pons J. A., Reddy S., Prakash M., Lattimer J. M., Miralles J. A., 1999, ApJ, 513, 780
Prendergast K. H., 1956, ApJ, 123, 498
Rea N., Esposito P., 2011, in Torres D. F., Rea N., eds, High-Energy Emission from Pulsars and their Systems. Springer-Verlag, Berlin, p. 247
Rheinhardt M., Geppert U., 2005, A&A, 435, 201
Roumeliotis G., Sturrock P. A., Antiochos S. K., 1994, ApJ, 423, 847
Ruiz M., Paschalidis V., Shapiro S. L., 2014, Phys. Rev. D, 89, 084045
Shafranov V. D., 1956, Sov. J. At. Energy, 1, 709
Spitkovsky A., 2006, ApJ, 648, L51
Spruit H. C., 2009, in Strassmeier K. G., Kosovichev A. G., Beckman J. E., eds, Proc. IAU Symp. 259, Cosmic Magnetic Fields: From Planets, to Stars and Galaxies. Cambridge Univ. Press, Cambridge, p. 61
Taverna R., Muleri F., Turolla R., Soffitta P., Fabiani S., Nobili L., 2014, MNRAS, 438, 1686

Thompson C., Duncan R. C., 1993, ApJ, 408, 194
Thompson C., Lyutikov M., Kulkarni S. R., 2002, ApJ, 574, 332
Tiengo A. et al., 2013, Nature, 500, 312
Turolla R., Esposito P., 2013, Int. J. Mod. Phys. D, 22, 30024
Viganò D., Pons J. A., Miralles J. A., 2011, A&A, 533, A125
Viganò D., Rea N., Pons J. A., Perna R., Aguilera D. N., Miralles J. A., 2013, MNRAS, 434, 123
Wilson J. R., Mathews G. J., 2003, Relativistic Numerical Hydrodynamics. Cambridge Univ. Press, Cambridge
Wilson J. R., Mathews G. J., Marronetti P., 1996, Phys. Rev. D, 54, 1317
Wolfson R., 1995, ApJ, 443, 810
Woods P. M., Kouveliotou C., Finger M. H., Göğüş E., Wilson C. A., Patel S. K., Hurley K., Swank J. H., 2007, ApJ, 654, 470
Yang W. H., Sturrock P. A., Antiochos S. K., 1986, ApJ, 309, 383
Yoshida S., Yoshida S., Eriguchi Y., 2006, ApJ, 651, 462

APPENDIX A: STRONG FIELD REGIME

Newly born magnetars, with their fast rotation (with period of the order of ∼1 s) and their strong magnetic deformation, can power a significant emission of GW and, during the first few seconds of their life, they could be a promising target for the next generation of ground-based GW interferometers (Mastrano et al. 2011). After this lapse of time, because of the spin-down induced by the strong poloidal field (∼10^{14} G) the strain amplitude reduces considerably and the GW emission is hardly detectable.

Even though our assumption of a force-free magnetosphere only applies to the late phases of a proto-NS, when GW emission will be quenched, it is still interesting to consider the strong field regime and how a magnetospheric distribution of currents acts on the stellar deformation. In the following, we will limit our discussion to sequences with $\lambda = 1.5$, considering only configurations with a simple topology with no detached magnetic flux rope outside the star. As discussed in Section 4, these kind of configurations, whose properties are weakly affected by λ, are possibly the only stable ones.

In the strong field regime, the solutions of the GS equation (7) depend on the specific value of the magnetic field strength and they do not rescale as in the weak-field limit. This is evident from Fig. A1, where we show the value of the ratio $B^{\rm pol}_{\rm max}/B_{\rm pole}$ as a function of $\hat{a}$ along sequences with constant value of $B_{\rm pole}$ (from the weak-field limit to ∼10^{17} G) and fixed gravitational mass $M = 1.551\,{\rm M}_\odot$. Just like in the weak-field regime, along each sequence the trend of $B^{\rm pol}_{\rm max}$

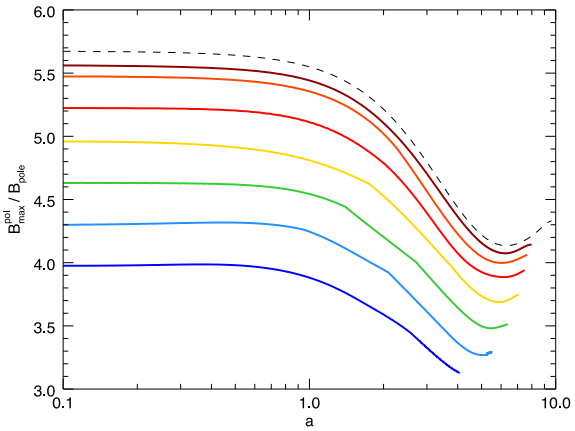

Figure A1. Profiles of the maximum value of the poloidal magnetic field $B^{\rm pol}_{\rm max}$ along sequences with $\lambda = 1.5$ and constant value of $B_{\rm pole}$. The solid lines from top to bottom $B_{\rm pole} = 0.2, 0.4, 0.6, 0.8, 1.0, 1.2, 1.4 \times 10^{17}$ G. The black dashed line corresponds to the weak-field limit.

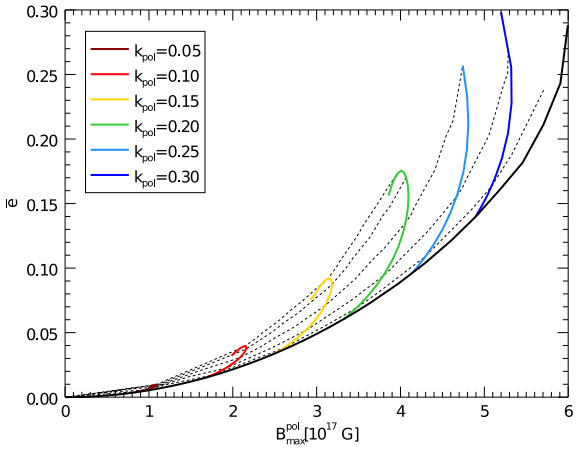

Figure A2. Profiles of the deformation rate $\bar{e}$ along sequences with constant value of $k_{\rm pol}$, $\lambda = 1.5$, and gravitational mass $M = 1.551\,{\rm M}_\odot$ as a function of the maximum value of the poloidal magnetic field $B^{\rm pol}_{\rm max}$. The black solid line represents the sequence with $\hat{a} = 0$ (purely poloidal configurations). The dotted lines correspond to sequences with fixed value of $\hat{a}$ equispaced from $\hat{a} = 1.0 \times 10^{-3}$ to 5.0×10^{-3}.

is not monotonic. Here, however, the ratio $B^{\rm pol}_{\rm max}/B_{\rm pole}$ is smaller for stronger magnetic fields. This can be explained in terms of the deformation of the star: as in the weak-field limit our equilibrium configurations are energetically dominated by the poloidal field (the magnetic energy ratio $\mathcal{H}_{\rm tor}/\mathcal{H}$ depends weakly on the strength of the field) and they show an oblate deformation. Therefore, if the star is more magnetized, the deformation is stronger and the pole is closer to the centre of the star implying a smaller $B^{\rm pol}_{\rm max}/B_{\rm pole}$.

Fig. A2 shows the deformation rate $\bar{e}$ (Kiuchi & Yoshida 2008; PBD14) as a function of $B^{\rm pol}_{\rm max}$. Here, the black lines trace the configurations with constant $\hat{a}$. Moving from the purely poloidal case with $\hat{a} = 0$ to higher value of $\hat{a}$ the toroidal magnetic field strengthen up to ∼2×10^{17} G and the deformation rate increases by a factor of ∼2. The presence of a toroidal field to the system, seems to increase, rather than reduce, the oblate deformation. However, as discussed in PBD14, neither the maximum strength of the magnetic field nor the magnetic energy is, in general, good indicator of the possible deformations of the NS. The distribution of the currents plays an important role and the effects of magnetic field located in the outer layers of the star are less important than those of comparable field situated in the core region. Therefore, the trend of $\bar{e}$ can be explained in terms of the strength of the poloidal magnetic field, which resides deeper inside the star. Moving along sequences with fixed $k_{\rm pol}$ (without constraints on $B_{\rm pole}$) from the purely poloidal configurations to higher $\hat{a}$, both the poloidal and the toroidal field grow in strength while the neutral line moves towards the surface of the star. Finally, as soon as the radius of the neutral line reaches a value of ∼$0.8 r_{\rm e}$, the poloidal field begins to drop leading to an inversion point in the sequences and a reduction of the deformation rate $\bar{e}$.

The deformation rate $\bar{e}$ has the advantage that it can be computed as an integral over the star, but it is strictly a Newtonian quantity. In GR, the relevant quantity for the emission of GW is the quadrupolar ellipticity $e_{\rm q}$ defined as

$$e_{\rm q} = -\frac{3}{2}\frac{I_{zz}}{I}, \tag{A1}$$

where I_{zz} is the gravitational quadrupole moment and I is the moment of inertia. The gravitational quadrupole moment cannot

be computed as an integral over the star but must be derived from the asymptotic structure of the metric terms (Bonazzola & Gourgoulhon 1996) in the limit $r \to \infty$. The moment of inertia can be properly defined only for rotating star as the ratio of the Komar angular momentum (Kiuchi & Yoshida 2008) over the rotational rate $I := \mathscr{J}/\Omega$ (Bonazzola & Gourgoulhon 1996; Frieben & Rezzolla 2012). For non-rotating stars, it can be evaluated in the limit $\Omega \to 0$:

$$I = \lim_{\Omega \to 0} \frac{\mathscr{J}}{\Omega} = \int (e + p)\psi^{10}\alpha^{-1}r^4 \sin^3\theta \mathrm{d}r\mathrm{d}\theta\mathrm{d}\phi. \quad \text{(A2)}$$

We find that in all our models the quadrupolar ellipticity is an almost constant fraction of the deformation rate: $e_\mathrm{q}/\bar{e} = 0.40 \pm 0.05$ (the uncertainty is mostly due to the asymptotic extrapolation of the metric terms). This agrees with what was already found by Frieben & Rezzolla (2012).

This paper has been typeset from a TEX/LATEX file prepared by the author.